Bioactive Materials 10 (2022) 1–14

Contents lists available at ScienceDirect

Bioactive Materials

journal homepage: www.sciencedirect.com/journal/bioactive-materials

MicroRNA-activated hydrogel scaffold generated by 3D printing accelerates bone regeneration

Ting Pan [a,b], Wenjing Song [a,c,d,*], Hongbao Xin [b], Haiyue Yu [f], He Wang [e], Dandan Ma [e], Xiaodong Cao [a,c,d], Yingjun Wang [a,c,d,**]

[a] School of Materials Science and Engineering, South China University of Technology, Guangzhou, 510006, PR China
[b] Institute of Nanophotonics, Jinan University, Guangzhou, 511443, PR China
[c] National Engineering Research Center for Tissue Restoration and Reconstruction, South China University of Technology, Guangzhou, 510006, China
[d] Key Laboratory of Biomedical Engineering of Guangdong Province, And Innovation Center for Tissue Restoration and Reconstruction, South China University of Technology, Guangzhou, 510006, China
[e] Department of Endodontics, Stomatological Hospital, Southern Medical University, No. 366 South Jiangnan Avenue, Guangzhou, 510280, China
[f] Charité–Universitätsmedizin Berlin, Corporate Member of Freie Universität Berlin, Humboldt-Universität zu Berlin, Berlin Institute of Health, Department of Oral Diagnosis, Digital Health and Health Services Research, Berlin, Germany

ARTICLE INFO

Keywords:
Bone repair
microRNA therapy
Scaffold
Osteogenesis

ABSTRACT

Bone defects remain a major threat to human health and bone tissue regeneration has become a prominent clinical demand worldwide. The combination of microRNA (miRNA) therapy with 3D printed scaffolds has always posed a challenge. It can mimic physiological bone healing processes, in which a biodegradable scaffold is gradually replaced by neo-tissue, and the sustained release of miRNA plays a vital role in creating an optimal osteogenic microenvironment, thus achieving promising bone repair outcomes. However, the balance between two key factors - scaffold degradation behavior and miRNA release profile - on osteogenesis and bone formation is still poorly understood. Herein, we construct a series of miRNA-activated hydrogel scaffolds (MAHSs) generated by 3D printing with different crosslinking degree to screened the interplay between scaffold degradation and miRNA release in the osteoinduction activity both *in vitro* and *in vivo*. Although MAHSs with a lower crosslinking degree (MAHS-0 and MAHS-0.25) released a higher amount of miR-29b in a sustained release profile, they degraded too fast to provide prolonged support for cell and tissue ingrowth. On the contrary, although the slow degradation of MAHSs with a higher crosslinking degree (MAHS-1 and MAHS-2.5) led to insufficient release of miR-29b, their adaptable degradation rate endowed them with more efficient osteoinductive behavior over the long term. MAHS-1 gave the most well-matched degradation rate and miR-29b release characteristics and was identified as the preferred MAHSs for accelerated bone regeneration. This study suggests that the bio-adaptable balance between scaffold degradation behavior and bioactive factors release profile plays a critical role in bone regeneration. These findings will provide a valuable reference about designing miRNAs as well as other bioactive molecules activated scaffold for tissue regeneration.

1. Introduction

Bone defects remain a major threat to human health and bone tissue regeneration has become a prominent clinical demand worldwide. However, bone formation is a complicated biological process which involves the interactions of both cells and bioactive factors. Increasing interest is being shown in tissue engineering to integrate cells and bioactive factors into a porous scaffold. Also attracting a great deal of attention for better tissue regeneration is the fabrication of the scaffold, which acts as a temporary extracellular matrix substitute for cell adhesion and neo-tissue formation. From this perspective, two requirements for scaffolds were therefore proposed for efficient bone defect regeneration [1]: (i) a precisely designed three-dimensional (3D) outer structure as well as a highly porous inner structure for cell/tissue infiltration,

Peer review under responsibility of KeAi Communications Co., Ltd.
* Corresponding author. School of Materials Science and Engineering, South China University of Technology, Guangzhou, 510006, PR China.
** Corresponding author. School of Materials Science and Engineering, South China University of Technology, Guangzhou, 510006, PR China.
E-mail addresses: phsongwj@scut.edu.cn (W. Song), imwangyj@scut.edu.cn (Y. Wang).

https://doi.org/10.1016/j.bioactmat.2021.08.034
Received 6 April 2021; Received in revised form 30 August 2021; Accepted 31 August 2021
Available online 3 September 2021

transport of nutrients, oxygen and metabolic waste; (ii) biodegradability with a controllable degradation to provide space for neo-tissue growth. 3D plotting technology using computer-aided design (CAD) and computer-aided manufacturing (CAM) shows great promise to address the first issue, since this technology can fabricate scaffolds with predetermined architectures, including an outer structure, inner pore size, porosity, and pore connectivity [2]. Using 3D plotting techniques, the geometry of scaffolds can be precisely designed to meet the optimized requirements for bone tissue regeneration [3–5].

To address the second issue, biodegradable polymers, especially natural hydrogels, have been identified as practical materials for biomedical application. Owing to their good biocompatibility, high moisture content and good permeability, hydrogels can provide a favorable microenvironment to support osteogenesis [6,7]. Moreover, the degradation rate of hydrogels can be precisely controlled by the crosslinking degree to match the growth rate of neo-tissue formation. Gelatin is denatured collagen, which is widely used for biomedical applications [8,9]. As a temperature-sensitive hydrogel, gelatin is suitable for printing and shaping through a sol-gel transformation [8]. Alginate is a natural hydrogel with excellent biomedical properties like biocompatibility and ionotropic gelation with divalent cations [10]. Thus, a porous gelatin-alginate scaffold generated by 3D plotting techniques shows great promise to serve as a desirable candidate for bone regeneration [11,12]. However, one critical drawback - the lack of osteoinduction activity - makes it difficult to precisely control and accelerate the osteogenesis process.

To improve the osteoinduction activity of scaffolds, various specific bioactive molecules have been loaded in or on these scaffolds to regulate the fate of stem cells and osteogenic differentiation process. MicroRNAs (miRNAs), the key post-transcriptional regulators of gene expression, have gained great attention for use in regenerative medicine applications because of several significant advantages: they are easy to synthesize and manipulate; they regulate the behavior of cells, specifically from the gene level; and their sequence is often completely conserved among species [13]. Furthermore, many studies have demonstrated the osteoinductive nature of miRNAs [14–17]. For example, it is well documented that miR-29b serves as a key regulator for the development of the osteoblast phenotype [18–20]. Therefore, the incorporation of miRNAs of interest into a biodegradable scaffold -to form an miRNA-activated scaffold (MAS) - offers a promising strategy to direct cell fate and promote the formation of extracellular matrix, which facilitates bone regeneration. Ma et al. developed miRNA-loaded PLGA microsphere scaffolds that could initiate cell repair and bone rebuilding mechanisms, with efficacy that could last for more than 4 weeks [21]. In another study, a light-crosslinkable gelatin-PEG hydrogel was employed for *in situ* miRNA delivery to promote the osteogenesis of mesenchymal stromal cells (MSCs) [9]. These studies demonstrate the enormous potential for future use of MASs for bone regeneration. Commonly, the sustained release of miRNA from an MAS was achieved by the degradation of the scaffold. However, the joint influence of the miRNA release

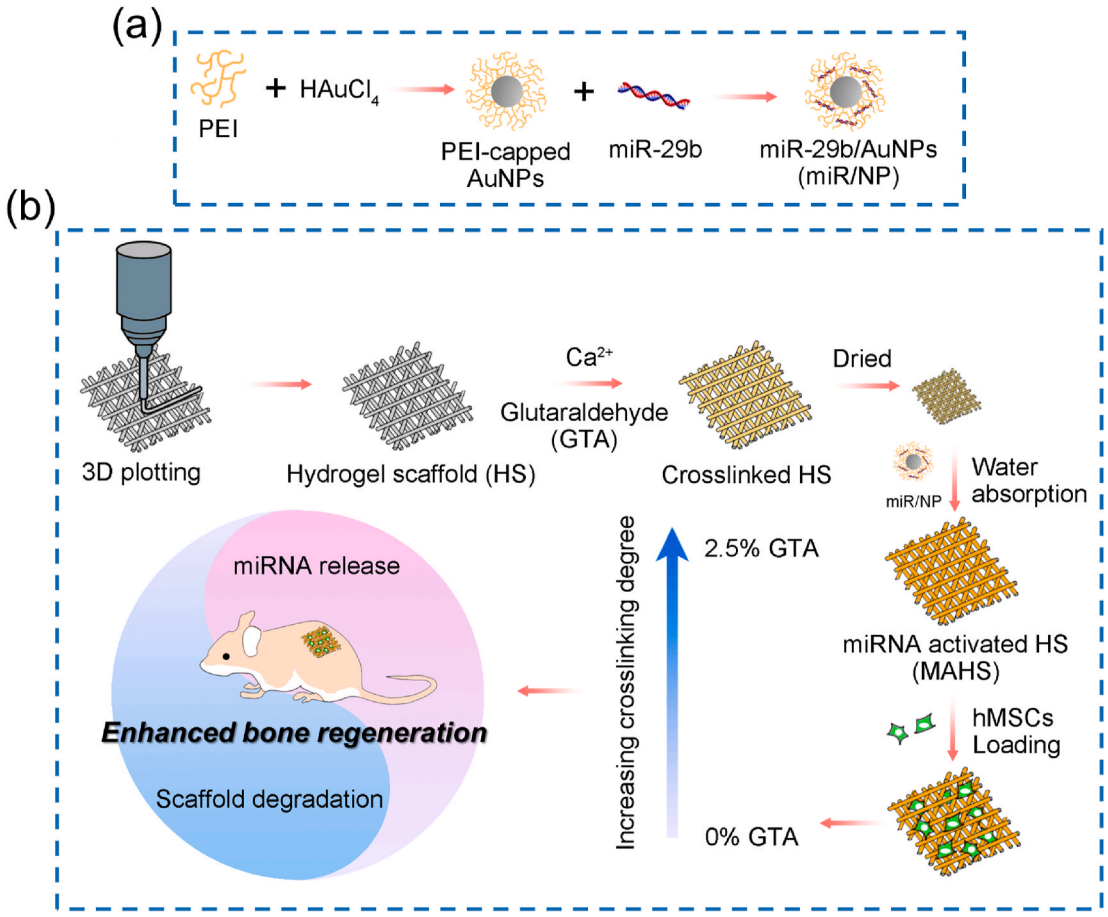

Fig. 1. Schematic diagram of MAHS preparation and function for osteogenesis and bone regeneration. (a) Illustration of miRNA nano-delivery system. PEI-capped AuNPs are synthesized through a convenient one-pot method. miRNAs were incubated with AuNPs to form stable complexes "miR/NP". (b) 3D porous hydrogel scaffold consisting of gelatin and alginate is generated layer by layer through a 3D plotting technique, then crosslinked with Ca^{2+} and varying concentrations of GTA. The lyophilized scaffold is subsequently immersed in miR/NP-containing PBS to load miR/NP through water absorption by the dried hydrogels. Finally, MAHSs with different crosslinking degree are applied for osteogenesis *in vitro* and bone formation *in vivo*, and this study focuses on the balance between the scaffold degradation rate and miRNA release profile.

profile and scaffold degradation behavior - which itself alters the miRNA release and is closely related to neo-tissue formation - on osteogenesis and new bone formation is still poorly understood.

In this study, we aimed to construct a series of miRNA-activated hydrogel scaffolds (MAHSs) and reveal the influence of the balance between miRNA release and scaffold degradation on osteogenesis of human bone mesenchymal stem cells (hMSCs) and bone regeneration (Fig. 1). The bioactive factor, miR-29b, was combined with a nano-delivery vector, polyethyleneimine (PEI)-capped gold nanoparticles (AuNPs) to form miR-29b/AuNPs nano-complexes (hereafter referred to as "miR/NPs" for short). The hydrogel scaffolds were fabricated by a 3D plotting technique using a mixture of gelatin and alginate, and they were crosslinked with Ca^{2+} and different concentrations of glutaraldehyde (GTA) to obtain scaffolds with different degradation rates. Then, the miR/NPs were loaded as releasable drugs inside each scaffold using the water swelling ability of hydrogels. Hydrogel scaffolds provided localized and sustained delivery via controlled release of loaded miRNA/AuNPs complexes, while AuNPs protect and enable efficient cytosolic accumulation of miRNA. The test results regarding scaffold performance influenced by the balance between the scaffold degradation rate and miRNA release profile were presented. Then, by observing *in vitro* osteogenic differentiation of hMSCs as well as *in vivo* bone formation, the performance of each MAHS was evaluated. Furthermore, our studies demonstrate that the balance between miRNA (or other bioactive factors) release and scaffold degradation should be carefully considered when designing regenerative scaffolds.

2. Experimental

2.1. Materials

The human miR-29b mimics (sequence: 5′-UAGCACCAUUUGAAAUCAGUGUU), their negative scrambled (miR-NC) controls (sequences: 5′-UUCUCCGAACGUGUCACGUTT) and Cy3-labeled miR-29b were obtained from GenePharma Co. Ltd. (Shanghai, China). High-viscosity sodium alginate (biochemical grade, Mw = 398.3) and gelatin (for microbiology, gel strength ~ 250 g) were purchased from Aladdin. Branched polyethylenimine (PEI, Mw 25 kDa), glutaraldehyde (GTA, 25 wt%) was purchased from Sigma-Aldrich. $HAuCl_4$ was purchased from Sinopharm Chemical Reagent Co., China. Quant-iT RiboGreen was purchased from Thermo Fisher. DAPI was purchased from Beyotime, China.

2.2. Cell culture

The hMSCs, purchased from Cyagen Biosciences Inc., China., were propagated in conventional growth medium (Cyagen Biosciences Inc.), consisting of hMSCs basal medium, 10% (v/v) fetal bovine serum (FBS), 100 mg/mL penicillin-streptomycin, and glutamine at 37 °C in a humidified atmosphere consisting of 5% CO_2. Cells from early passages (≤6) were used for all experiments.

2.3. Preparation and characterization of miRNA/AuNPs nano-delivery system

PEI-capped gold nanoparticles were employed as miRNA carrier, and prepared through a convenient one-pot procedure as previously described [22]. Briefly, 2 ml of 14 mM $HAuCl_4$ was mixed with 1.44 mL of 1% (w/w) branched PEI and stirred at room temperature for 24 h. The products were centrifugated, rinsed with DEPC water to remove unreacted species. To identify the optimal miRNA/AuNPs ratio, miR-29b (1 pmol) was mixed with PEI-capped AuNPs at various weight ratio for 15 min at room temperature to form miR-29b/AuNPs nanocomposites, then a 1% (w/v) agarose gel retardation assay was performed to assess the binding ability of AuNPs to miRNA.

The morphology of AuNPs was examined using transmission electron microscopy (TEM; JEM-2100HR, Japan). UV–vis spectra of AuNPs were obtained with a Persee TU-1901 UV–vis absorption spectrometer (China). Size distribution and zeta potential of AuNPs and miR-29b/AuNPs were determined by using Dynamic Light Scattering (DLS) and the Malvern Zetasizer Nano ZS90 instrument (Malvern, UK), respectively. Atomic force microscope (AFM, MFP-3D-S, Bruker, USA) was performed to examine the morphology of miR-29b/AuNPs.

Intracellular delivery efficacy of miR-29b/AuNPs was assessed by confocal laser scanning microscopy (CLSM, Leica TCS SP8, Germany) and flow cytometry (Guava easyCyte, Merck). Cy3-labeled miR-29b (100 pmol, 1.41 μg) were mixed with 4.23 μg of AuNPs (AuNPs/miR-29b weight ratio = 3:1), then added to hMSCs cells at a final miRNA concentration of 50 nM in Opti-MEM (Invitrogen). After incubation for 8 h, cells were extensively washed with cold PBS and fixed with 4% formaldehyde for 30 min. After rinsing twice with PBS, cells were immersed first in 0.1% Triton X-100 for 10 min to increase permeability, then stained with Cell Navigator F-Actin Labeling Kit (AAT Bioquest Inc.) for the cell skeleton (green fluorescence), and finally, 4′,6′-diamidino-2-phenylindole (DAPI, Beyitime, China) for the cell nucleus (blue fluorescence). Slides were mounted and observed using CLSM. For flow cytometry analysis, transfected cells were detached using trypsin and resuspended in ice cold PBS for evaluation on a flow cytometer (Guava easyCyte, Merck Millipore, USA). The transfection efficiency was represented as the percentage of fluorescence positive cells at an excitation wavelength of 550 nm.

The cytotoxicity of miR-29b/AuNPs were evaluated by CCK-8 assay (Dojindo, Japan) and live/dead staining assay. Briefly, hMSCs cells were seeded in 96-well plates at a density of 5000 cells per well and incubated overnight. Then, the medium was changed to growth medium containing free miR-29b, AuNPs, or miR-29b/AuNPs complexes (50 nM), respectively. At the indicated times, cells were incubated with CCK-8 working solution for 1 h at 37 °C, then the absorbance of supernatant at 450 nm was measured with a microplate reader (Thermo3001, Thermo).

For live/dead cell staining assay, hMSCs were seeded in a 48-well plate at a density of 1×10^4 cells per well and incubated overnight. After incubated with different formulations at an equal concentration of 50 nM for 24 h or 48 h, cells were washed with PBS, then stained with calcein-AM and PI solutions in PBS and incubated for 30 min at room temperature to differentiate the live and dead cells. Finally, cells were washed three times with cold PBS and observed on the fluorescence microscope.

2.4. Fabrication of 3D plotted gelatin-alginate scaffolds

The porous scaffolds were produced using a 3D plotting technique as reported in our earlier publication [8]. Briefly, gel inks were prepared by mixing 4 wt% alginate and 20 wt% gelatin in DI water to form a uniform solution. Hydrogel ink was pre-heated at 50 °C to form sol and then loaded into a syringe with a 400 μm nozzle. 3D scaffolds were fabricated by printing the inks using a Bioplotter™ device (Envisiontec GmbH, Germany). The printing temperature was 37 °C and bed temperature was 10 °C. Scaffolds with knitted porous structure (10.0 mm in diameter, 2.0 mm in thickness) were printed as designed (Magics X, Materialise Software) with 2 mm/s printing speed, rectilinear fill pattern and 0.32 mm layer height. After printing, the samples were sequentially immersed in 0.5 μM of $CaCl_2$ for 10 min and GTA with different concentration (0, 0.25, 1, 2.5 wt%) for 30 min to crosslink alginate and gelatin respectively. Then, scaffolds were dialyzed to remove the excess GTA. Finally, scaffolds were lyophilized at −20 °C for 48 h for further use.

2.5. Construction and characterization of MAHS

The lyophilized 3D porous scaffolds were first sterilized by ultraviolet radiation. Subsequently, the sterile scaffolds (10 mm × 10 mm × 2

mm) were immersed in 180 μL serum-free Opti-MEM containing miRNA/AuNPs nanocomplexes (with miRNA concentration of 60 μM) at 4 °C overnight. Afterwards, the scaffolds were air-dried at room temperature. The loading content of miRNA in each MAHS was 135 μg.

The geometry and architecture of the MAHS were observed by three-dimensional rotational optical microscopy (HiroX7700, HiroX, Japan). The surface morphology of scaffolds was characterized using scanning electron microscopy (SEM, Nova Nano 430, FEI, Netherlands). The 3D distribution of miRNA/AuNPs were observed with laser scanning confocal microscope (LSCM) by labelling miR-29b with red fluorescence Cy3.

To assess the mechanical properties of each miRNA-loaded hydrogel scaffolds, the compressive stress-strain measurements were performed on the water swollen printed hydrogels using a dynamic mechanical analysis (DMA, Q800DE, TA Instruments, USA). The rectangular block hydrogel scaffolds (10 mm × 10 mm × 2 mm) were precisely measured using a digital caliper micrometer. The stress-strain curves of the scaffolds were recorded at a compressing speed of 1 mm/min, and the compressive modulus was derived from the regression of the linear portion of stress-strain curves. Each measurement was performed in quintuplicate. Results are reported as the mean standard deviation.

To monitor the water swelling ability of each scaffold, the pre-weighed dried scaffolds were immersed in distilled water for 24 h at 37 °C in a shaking table. The weight change of each scaffold was monitored at different time intervals. Swelling ratio (Q) was calculated as

$$Q\ (\%) = W'\ /W_0 \times 100$$

where W' and W_0 represent the final and initial weight of scaffold, respectively. For each group, five samples were used for measurement and average data were used for calculations.

The degradation rate of each scaffold was calculated by soaking sterilized scaffolds in Dulbecco's modified Eagle's medium, supplemented with 10% fetal bovine serum, and incubated in an atmosphere of 5% CO_2 at 37 °C. At different time intervals, the scaffolds were taken out and weighted after lyophilization. The medium was changed every second day, and scaffolds were incubated for 15 days. The degradation was calculated as

$$\text{Degradation}\ (100\%) = (W_0 - W')/W_0 \times 100\%$$

where W' and W_0 represent the final and initial weight of scaffold, respectively. For each group, five samples were used for measurement and average data were used for calculations.

2.6. In vitro miRNA release study

The release profiles of miRNA-loaded 3D-gel scaffolds were examined in sterile PBS (pH 7.4, 0.1 M). For miRNA releasing assay, the MAHS was cutted into four small pieces with the same size. The loading content of miRNA in each diced piece was 33.75 μg. The scaffolds were placed in 2 ml PBS and shaken at 50 rpm. at 37 °C. At predetermined time intervals, 200 μL release medium was withdrawn and replaced with pre-warmed fresh PBS. Quant-iT RiboGreen working solution (100 μl) was added to each well in a 96-well plate containing 100 μl of unknown, blank or standard sample, and mixed briefly. After being incubated for 5 min at room temperature (protected from light), the miRNA concentration of the sample was measured using a ThermoElectron 3001 Varioskan Flash Spectral Scanning Microplate Reader. The miRNA release was calculated as

$$\text{Fractional miRNA release} = m'/m_0$$

where m' represents the miRNA amount at detected time point, and m_0 represents the initial weight of miRNA loaded on scaffold. For each group, five samples were used for measurement and average data were used for calculations.

2.7. Cell adhesion on scaffolds

hMSCs were seeded on scaffolds at a density of 2×10^5 cells/scaffold. After 24 h of incubation, the scaffolds with cells cultured on them were washed with PBS, fixed in 2.5% glutaraldehyde, dehydrated in a graded ethanol series and freeze-dried. After sputter coating with gold powder, the cell morphology was observed by the FE-SEM.

2.8. Biomineralization on MAHS

To monitor the biomineralization on the surface of MAHS, sterile scaffold was immersed into complete cell culture medium (DMEM+10% FBS), and the medium was changed every second day. After 5 days of immersion, the scaffold was washed three times with PBS, and then freeze-dried. The surface morphology of scaffold and formed mineralized apatite crystals were observed by SEM. Elemental analysis of mineralized nanoparticles was monitored by energy dispersive X-ray spectroscopy (EDS, Nova Nano 430, FEI, Netherlands).

To compared the influence of hydrogel crosslinking degree on scaffold mineralization, each mineralized scaffold was totally degraded by aqua regia, and the representative elements for mineralization, P and Ca elements in each MAHS were monitored with inductively coupled plasma-mass spectrometry (ICP-MS, NexION 350, PerkinElmer, U.S.A).

2.9. In vitro study of osteogenic gene expressions by qRT- PCR

Osteoblastic differentiation was confirmed via qRT-PCR examination of marker genes: Runt-related transcription factor 2 (Runx2), alkaline phosphatase (ALP), type I collagen (Col-I), osteocalcin (OCN). The cells were seeded onto MAHS in 24-well plates at a density of 2×10^5/scaffold. After 24 h incubation, the medium was altered to osteogenic medium. At the specified time-points, total RNA was isolated using the Trizol reagent (Invitrogen, USA) and quantified with a NanoDrop2000 spectrophotometer (Thermo Scientific, USA). RNA was reverse-transcribed into cDNA using a PrimeScript® RT reagent Kit with gDNA Eraser (TaKaRa Biotechnology, Japan), according to the manufacturer's instructions. Quantitative real-time PCR (qRT-PCR) analysis was performed on a RT-PCR instrument (QuantStudio™ 6 Flex, Life Technologies, USA) using the SYBR Green System (GeneCopoeia, USA) by the comparative cycle threshold (CT) method. Gene expression data were normalized to GAPDH and calculated using the $2^{-\Delta\Delta Ct}$ method. The primer sequences used for amplification are presented in Table S1.

2.10. Animal experiments

Male BALB/c athymic nude mice (6–8 weeks old, weighing ~18–22 g) were obtained from the Charles River Laboratories, Institute of Laboratory Animal Sciences, Chinese Academy of Medical Science (Beijing, China), and routinely acclimated for one week in the animal facility at South China University of Technology (SCUT) before initiation of experimental procedures. The animal experiments were performed following a protocol approved by the Institutional Animal Care & Use Committee at the SCUT.

After MAHSs with different crosslinking degrees were established, each scaffold was seeded with 2×10^5 hMSCs cells and incubated *in vitro* for 14 days, and then implanted in subcutaneous pockets on the back of nude mice. Briefly, mice were anaesthetized with 2% inhalation of isoflurane. Two dorsal midsagittal incisions were made on the disinfected back. One subcutaneous pocket was created on each side of each incision using blunt dissection, and one scaffold was implanted into each pocket. Four samples were implanted randomly for each group (n = 4). For bone-formation examination, the implants were harvested at 2, 4, and 8 weeks for subsequent H&E or immunofluorescence staining and micro-CT analysis.

2.11. Bone histological and immunohistochemical staining analysis

The specimens from subcutaneous implantation were fixed in 4% neutral buffered formalin and decalcified in 10% EDTA for 10 days at room temperature. Then, specimens were subsequently embedded in paraffin and cut into 5-μm thick sections. Hematoxylin and eosin staining (H&E) were used for histomorphometric analysis.

For immunofluorescence analysis of OCN or vascular endothelial growth factor (VEGF) expression in newly formed tissues, the slides were de-paraffinized and cooked in citrated buffer (2.1 M citric acid, pH 6.0) at 120 °C for 30 min for antigen retrieval. After blocking in serum, the sections were incubated overnight at 4 °C with a rabbit polyclonal primary antibody to OCN (1:100, CTS) or a rabbit monoclonal primary antibody to VEGF (1:100, CTS). After three washes in PBS, the sections were incubated with FITC-conjugated donkey antibody to rabbit IgG (1:400, CTS) for 1 h. The sections were mounted with the medium containing DAPI and then examined under a confocal microscope.

2.12. Micro-computed tomography (μCT) analysis

Micro-CT analysis was used to estimate volume of bone regeneration within the cell-laden MAHS. After 8 weeks of implantation, scaffolds were harvested and fixed in 4% neutral buffered formalin. Then samples were transferred to PBS and scanned using a μCT system (SKYSCan1176, Germany) at high resolution (17.4 μm voxel size), with X-ray energy of 59 kV and intensity of 167 μA, and exposure time of 300 ms. Analyses were performed with three-dimensional reconstruction software Data Viewer V1.5.1 and tissue analysis software CT Analyser V1.14.4. New bone volume fraction (bone volume/total volume, BV/TV) was analyzed in a volume of interest (VOI) including whole scaffolds.

2.13. Statistical analysis

All experimental data were presented as means ± standard deviations. The one-way analysis of variance (ANOVA) and independent samples *t*-test were used to determine the level of significance. $P < 0.05$, 0.01, and 0.001 was set to be significant, highly significant, and extremely significant, respectively.

3. Results and discussion

3.1. Characterization of miR-29b/AuNPs nano-delivery system

Despite great potential, the full implementation of miRNA therapeutics in the clinic is hampered by inefficient intracellular delivery due to susceptibility to RNase degradation, inefficient membrane

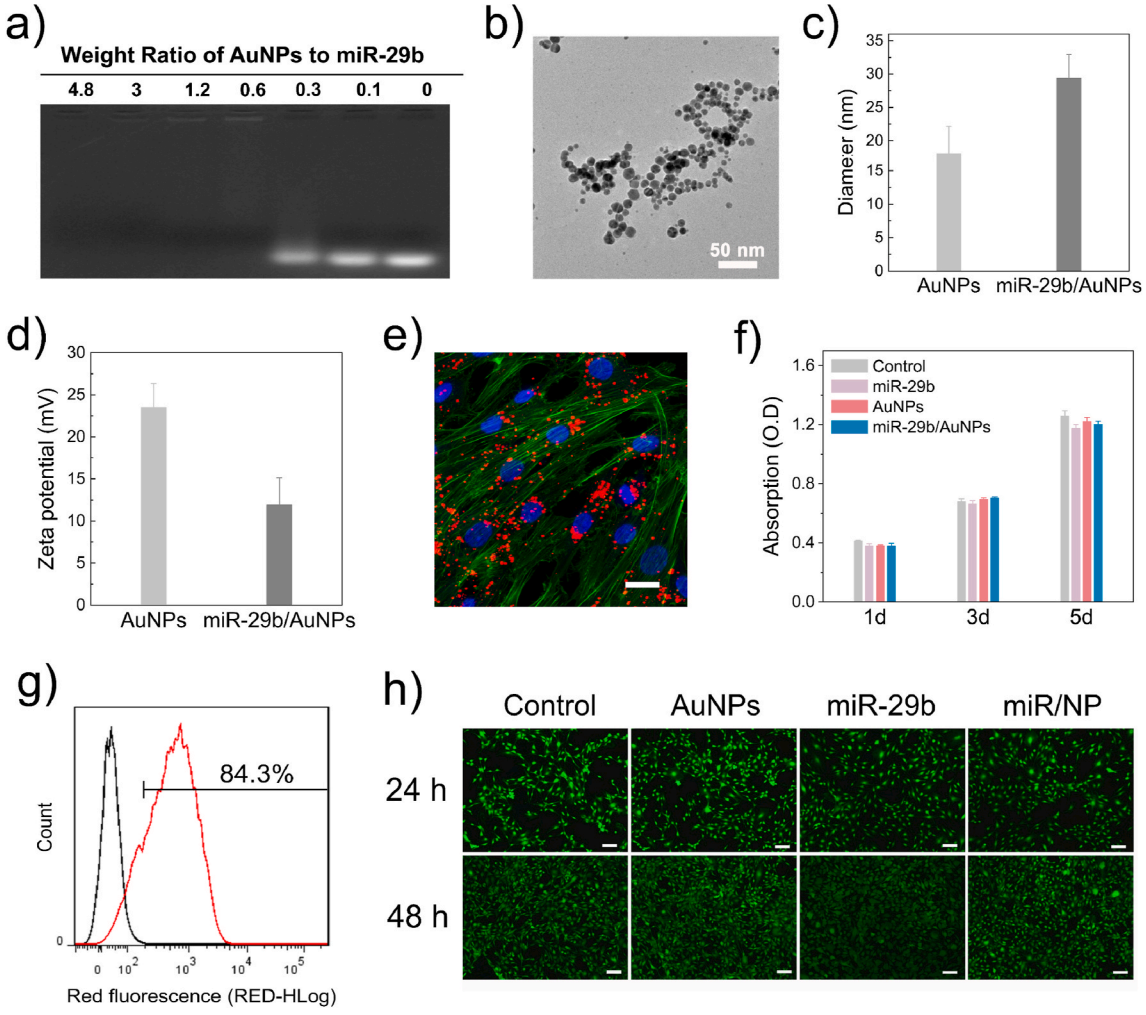

Fig. 2. Characterization of miR-29b/AuNPs (miR/NP) nano-delivery system. (a) Electrophoretic retardation analysis of miR-29b binding ability to AuNPs. (b) TEM image of miR/NP. (c) Hydrodynamic size and d) Zeta potential of AuNPs and miR/NP. (e) Intracellular delivery of Cy3-labeled miR/NP in hMSCs observed by confocal microscopy. (f) Cytotoxicity assay of hMSCs treated with different formulations detected by CCK-8 assay. (g) Cy3-positive cells treated with Cy3-miR/NPs detected by flow cytometry. (h) Fluorescence images of hMSCs co-stained by Calcein AM and PI treated with different formulations after 24 h and 48 h. Scale bar: 100 μm. Data are mean ± s.d., n = 5 per group.

penetration, and poor tissue-specific localization [14]. Therefore, the first step in constructing the MAHS is to design a nano-system for efficient intracellular miRNA delivery. Considering the excellent delivery performance of miRNA/siRNA in several reported studies, PEI-capped AuNPs (named "AuNPs" for short) were employed as a nano-vector for miR-29b intracellular delivery in this study (Supplementary Fig. S1) [22–24]. The miR-29b/AuNPs complexes were prepared via electrostatic interactions by incubating a mixture of miR-29b and AuNPs. When the weight ratio of AuNPs/miR-29b reached 0.6, a complete retardation of miRNA migration in agarose gel electrophoresis was achieved, indicating the effective condensation of negatively charged miR-29b on AuNPs (Fig. 2a). The miR/NP had a uniform spherical morphology with diameter of about 25 nm observed by TEM and AFM (Fig. 2b and Supplementary Fig. S2). The average hydrodynamic radius of miR/NP acquired by dynamic light scattering (DLS) was at around 29.3 nm, obviously increased compared to AuNPs (around 18.1 nm) due to the formation of miR/NP complexes from well-distributed AuNPs colloids (Fig. 2c). The zeta potential of the positive charged AuNPs decreased from +23.5 to +11.9 mV (Fig. 2d), reflecting the successful binding of miR-29b on the surface of AuNPs.

The ability of nano-vectors to ferry miRNA through the cell membrane is crucial for successful gene regulation. To assess the intracellular delivery efficiency of miR/NP, miR-29b was labeled with red fluorescence Cy3 and miR/NP-transfected hMSCs were analyzed by confocal microscopy and fluorescence-activated cell sorting (FACS). As shown in Fig. 2e, large amounts of red fluorescence signals were observed in hMSCs close to the nucleus after incubation with Cy3-miR/NP for 8 h, indicating efficient cellular uptake of miR/NP. Specifically, the intracellular delivery efficiency quantified by FACS was recorded as up to 84.3% (Fig. 2g), signifying that AuNPs delivered miR-29b into the cytoplasm with relatively high efficiency. Moreover, low cytotoxicity is a prerequisite for delivery vectors. Cytotoxicity assays (CCK-8 and live/dead staining) demonstrated that both AuNPs and miR/NP exhibited excellent biocompatibility with more than 95% viability for 5 days compared to untreated cells (Fig. 2f and h). Taken together, these results confirmed that the miR/NP nano-delivery system gave excellent intracellular delivery efficiency with negligible cytotoxicity, thus providing a simple and effective strategy to deliver miRNA to hMSCs.

3.2. Construction of MAHS

The 3D porous hydrogel scaffolds, consisting of 20 wt % gelatin and 4 wt % alginate, were constructed by a 3D plotting technique we have previously described [8]. Considering that the degradation rate of a scaffold is directly determined by the crosslinking degree of the hydrogels, scaffolds were crosslinked with $CaCl_2$ (0.5 μM) and different concentration (0, 0.25, 1, 2.5 wt%) of glutaraldehyde (GTA) to obtain scaffolds with different crosslinking degrees. The loading of miR/NP into the as-prepared 3D porous scaffolds was realized by immersing the lyophilized scaffolds into an aqueous miR/NP solution. The absorption of miR/NP was accompanied by the rapid and dramatic swelling of the hydrogels. To study the influence of the balance between scaffold degradation and miRNA release profile on osteogenesis of hMSCs and bone formation, miR/NP loaded on scaffolds with different crosslinking degrees were prepared (named as MAHS-0, MAHS-0.25, MAHS-1 and MAHS-2.5, respectively), and then lyophilized for further study.

The overall structure of each MAHS in the dried state was characterized by 3D optical microscopy. As shown in Fig. 3a, all scaffolds had uniform structures with interconnected macro-scale pores. The porosity of each MAHS was determined by micro-CT to be about 72%, and the pore connectivity was close to 100%. The pore size of all MAHSs was about 400 μm. There were no noticeable variations in the porosity, pore

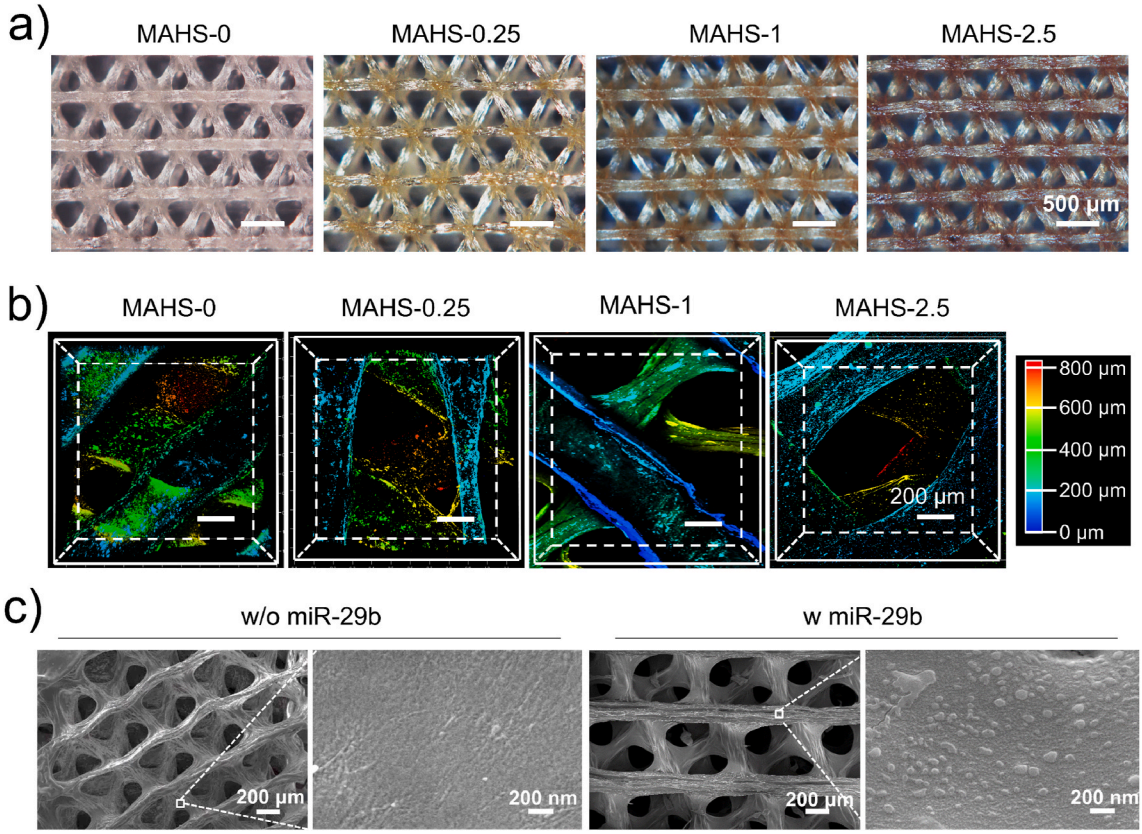

Fig. 3. Structure and morphology of MAHSs crosslinked with different concentrations of GTA. a) Optical images of each MAHS observed by 3D rotational microscopy. b) 3D distribution of miR/NP in MAHSs observed and reconstructed by confocal microscopy. miR-29b were labeled by Cy3. c) SEM images of MAHS-1 with and without miR/NP loading.

connectivity and pore size among MAHSs with different crosslinking degrees. With the increase of GTA concentration, the color of the scaffold fibers gradually deepened from light yellow to dark brown. In general, the yellow/brown coloration stems from the reaction of NH_2 groups of amino acids in gelatin with the C═O group of the GTA, resulting in a Shiff base [25]. Accordingly, with the increase of GTA concentration, the increased color intensity confirmed more Shiff bases formation, thus proving the increased crosslinking degrees. These result agreed well with other reports associated with GTA-crosslinked gelatin [26–28].

To further study the 3D distribution of miR/NPs on the scaffolds, Cy3-labeled miR-29b were applied and scaffolds were scanned layer by layer using confocal microscopy. As shown in Fig. 3b, the miR/NP complexes were homogeneously distributed in all MAHSs, confirming the favorable drug loading capacity of 3D-plotted hydrogel scaffolds. The surface morphology of scaffolds before and after miRNA loading was characterized by scanning electron microscopy (SEM). Taking the MAHS-1 as an example, unmodified scaffold showed a flat and smooth surface morphology (Fig. 3c). In contrast, numbers of nanoclusters were observed on the surface of MAHS-1, indicating the attachment of miR/NP complexes on the surface of the scaffold fibers. Due to dehydration, the nano-complexes agglomerated to form clusters with a particle size of about 100 nm. Energy Dispersive Spectrum (EDS) analysis showed that in addition to the C, O and N elements of the hydrogels, P and Au elements belonging to the miR/NP complexes could also be detected, proving that these nanoclusters were truly miR/NP and were stably loaded onto the scaffolds (Supplementary Fig. S3). The uniform distribution of the miR/NP in the MAHSs made it possible to predict the stable and continuous release of the miR-29b.

3.3. Mechanical properties of MAHS

Appropriate mechanical strength is a vital requirement for tissue engineering scaffolds. Natural hydrogels usually have weak mechanical properties which are not sufficient to meet the requirements of tissue repair. The modification in a restricted scope by chemical/physical crosslinking methods or composite strategies is simple and effective [29,30]. In this study, alginate was physically crosslinked with Ca^{2+} ions and gelatin was chemically crosslinked with different concentrations of GTA, which might alter the mechanical properties of MAHS. The compressive strength of each of the four MAHSs was measured in a hydrated state and calculated from the initial slopes of the typical compressive stress-strain curves (Fig. 4a). As shown in Fig. 4b, the compressive moduli of MAHS-0, MAHS-0.25, MAHS-1 and MAHS-2.5 were about 1.24, 2.08, 3.12 and 4.33 kPa, respectively. On the contrary, the final deformation of MAHSs decreased with increasing GTA concentration (Fig. 4c). These results demonstrated that increased crosslinking degree led to an obvious increase in the mechanical strength and stiffness of MAHS.

3.4. Water swelling and degradation behavior of MAHS

Water swelling ability is an important feature for tissue-engineered scaffolds, since it relates to the absorption of body fluid as well as diffusion and transport of nutrients and waste products. In the dry state, hydrogels can absorb water up to hundreds or even thousands of times their own weight to form a chemically stable or biodegradable colloid, thus making them very suitable for loading of drugs and bioactive factors. Regarding the swelling properties of MAHSs (Fig. 4d), the swelling ratios (Q) of MAHS-0 and MAHS-0.25 were 7.01 ± 0.41 and 5.61 ± 0.35, respectively. As the crosslinking degree increased, Q values of MAHS-1 and MAHS-2.5 significantly decreased to 3.91 ± 0.35 and 2.95 ± 0.23, respectively. All scaffolds had a relatively high swelling ratio, probably owing to the water absorption characteristics of hydrogels and 100% interconnected macropores of the scaffolds.

Biodegradation is another important factor. An ideal scaffold should be able to degrade with time *in vivo*, preferably at a controlled degradation rate and eventually creating spacing for the neo-tissue formation. The *in vitro* degradation of MAHSs in PBS (pH of 7.4) at 37 °C was

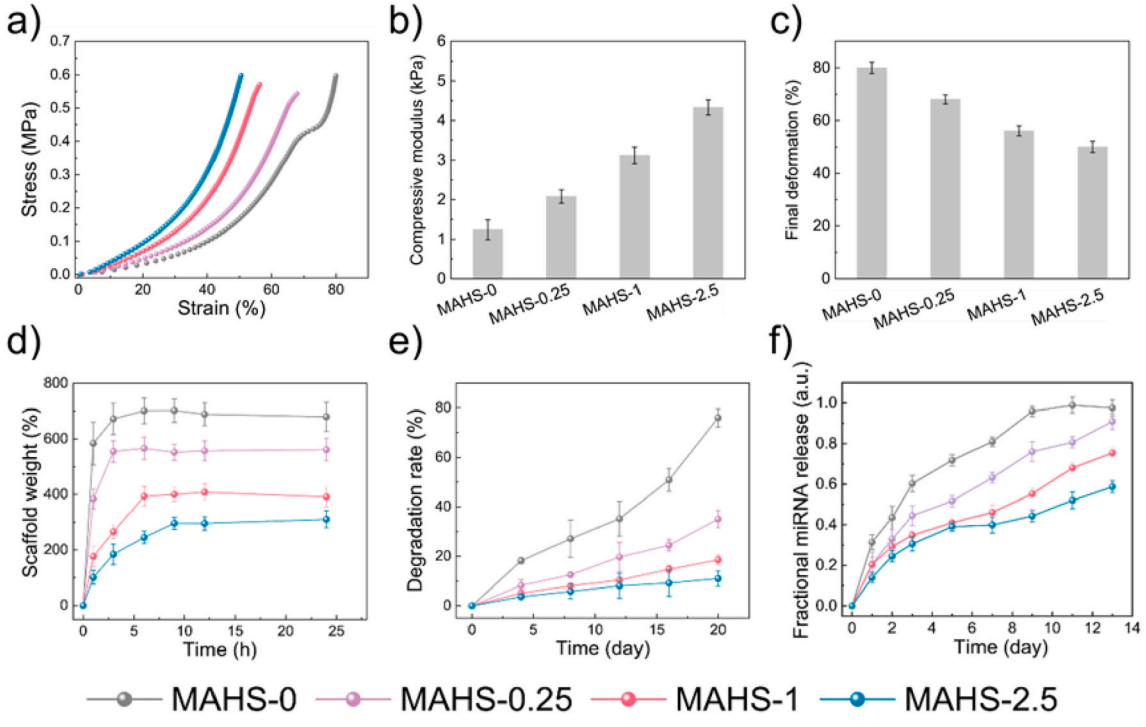

Fig. 4. Characterization of MAHSs crosslinked with different concentration of GTA. (a) Stress–strain curves of each MAHS monitored by dynamic mechanical analysis with a compression rate of 1 mm/min. (b) Compressive modulus and (c) final deformation of each MAHS calculate from the stress-strain curves. (d) Swelling ratio and (e) degradation rate of MAHSs with different crosslinking degree in PBS. (f) miR-29b releasing profile from each MAHS. Data are mean ± s.d., n = 5 per group.

examined in terms of their weight change (Fig. 4e). MAHS-0 and MAHS-0.25 degraded up to 80% and 37% at 20 days, respectively, while MAHS-1 and MAHS-2.5 degraded about 19% and 15%, respectively. These results indicate that increasing crosslinking degree leads to a decrease in degradation rate, which might affect the miRNA release as well as hMSCs behavior.

3.5. Release behavior of miRNA from MAHS

The release of miR/NP from MAHSs was monitored in PBS (Fig. 4f). With the increase in crosslinking degree, the release rate and amount of miRNA decreased, resulting a prolonged release behavior. This result was consistent with the degradation study, since the miR/NP release rate is closely related to hydrogel persistence. Additionally, a stable release action without burst release at an early stage was observed in all scaffolds, indicating controlled release behavior using the hydrogel scaffold system. We hypothesized that the sustained release profile was not only caused by the gradual degradation of scaffolds and the uniform distribution of miR/NP, but also partially because of the electrostatic interactions between positive charged miR/NP and negatively charged sodium alginate with abundant –COOH groups [31]. All in all, MAHSs with different crosslinking degree exhibited markedly different degradation rate and miRNA release behavior, which may have a significant influence on osteogenesis of hMSCs and bone formation.

3.6. Cell adhesion on MAHS

We then observed hMSCs adhesion and cell morphology after seeding on each MAHS for 48 h hMSCs were post-stained to purple for more intuitive observation. As shown in Fig. 5, spreading cells were hardly observed on MAHS-0, while most attached cells showed a rounded cell morphology. Cells spread slightly on MAHS-0.25, but no significant pseudopodal extension was observed. On the contrary, cells spread out with abundant lamellipodia and filopodia on MAHS-1 and MAHS-2.5, indicating that the morphology of hMSCs on the scaffold was dramatically affected by the crosslinking degree of hydrogel.

In the previous sections, we have demonstrated that the crosslinking degree of hydrogel greatly affects the mechanical properties of MAHS. Therefore, we speculated that the cell morphology and adhesion was likely affected by the stiffness of MAHSs. Although there is little research focused on the effect of mechanical properties of 3D scaffolds on cell morphology, there are many helpful studies based on 2D culture for reference. It is well documented in 2D culture studies that the stiffness of the microenvironment dramatically influences cell morphology, cytoskeletal structure, signaling, and function for many cell types. Higher stiffness substrates facilitate cell adhesion and spreading and help to form a more orderly cytoskeleton [32,33]. Indeed, we observed the spreading area of hMSCs increased with the increase in the stiffness of scaffolds. The results confirmed that the crosslinking degree of scaffolds had a crucial influence on cell morphology and adhesion.

3.7. In situ formation of calcium phosphate derivatives on the surface of MAHS

Interestingly, after 5 days of incubation, white particulate coatings were observed on the surface of the MAHSs (Fig. 6a). Taking MAHS-1 as an example, these white particulate coatings were observed to be mineral spheres under higher magnification (Fig. 6b), composed of plate-like crystallites (Fig. 6c), a typical morphology observed in crystalline apatite grown on bioactive glasses, polymer substrates, or collagen films using simulated body fluid (SBF) mineralization [34–36]. EDS analysis performed on the spherical aggregates confirmed the presence of calcium and phosphorus elements and the expected Ca/P ratio (1.78 ± 0.1), demonstrating that the spherical aggregates were mineralized apatite crystals (Fig. 5d).

We further compared the influence of hydrogel crosslinking degree on scaffold mineralization. The mineralized MAHSs were totally degraded by aqua regia, and the representative elements for mineralization of calcium and phosphorus in each MAHS-were measured with ICP. As shown in Fig. 5e, with increasing crosslinking degree of the

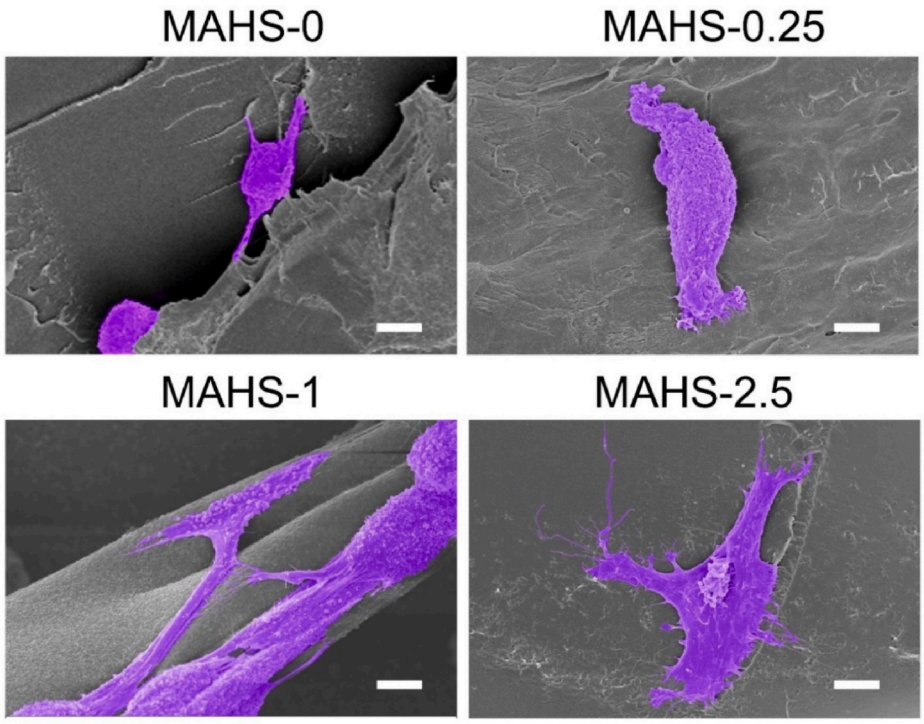

Fig. 5. SEM images of hMSCs adhesion and cell morphology on different MAHS after seeded for 2 days. Cells are pseudocolored with purple. Scale bar: 6 μm. (For interpretation of the references to color in this figure legend, the reader is referred to the Web version of this article.)

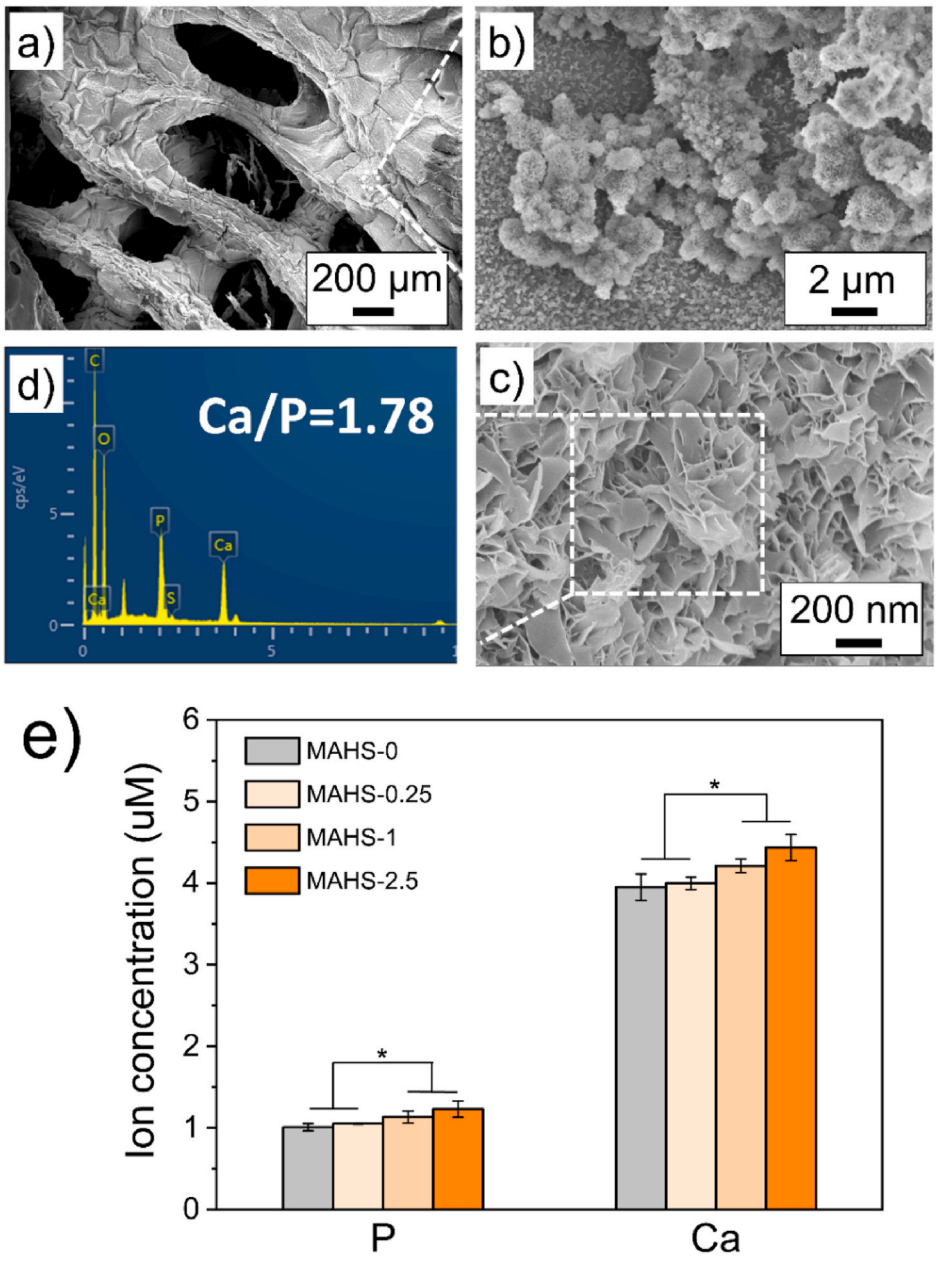

Fig. 6. Mineralization of MAHS. (a–c) SEM images of mineralized crystalline apatite on the surface of MAHS-1 with different magnifications after immersion in medium for 3 days. (d) EDS spectrum of mineralized MAHS-1. (e) Ion concentrations of calcium and phosphorus in each mineralized MAHS. Data are mean ± s.d., n = 4 per group.

scaffold, the calcium and phosphorus ion concentration slightly increased. This result indicated that the crosslinking degree of scaffolds has no significant effect on the mineralization process.

It is worth noting that this rapid mineralization process simply occurred in normal cell growth medium, rather than in SBF. We speculated that the rapid mineralization capacity of MAHSs is probably owing to the co-regulation of mineralization by gelatin and calcium ions chelated by alginate. As a denatured collagen derived from main part of the extracellular bone matrix, gelatin can offer nucleation sites that are quite similar to those of the biological matrix, which can induce the precipitation of hydroxyapatite [37]. In this study, The presence of calcium within the gelatin can provide abundant nucleation sites for the growth of Ca–P structures, thus facilitating the rapid mineralization of MAHS [38]. This rapid self-assembled mineralization process on the surface of MAHSs has potential to provide a niche of high ion concentrations to facilitate osteogenic differentiation of stem cells.

3.8. MAHS induced osteogenic differentiation of hMSCs in vitro

Osteogenic differentiation of hMSCs on each MAHS was monitored by measuring expressions of osteogenic phenotype markers using real-time PCR and Western blot (Fig. 7). MAHS-0 was not selected for further *in vitro* and *in vivo* studies, since it was difficult to evaluate the long-term effects due to the too fast degradation. hMSCs seeded on 1% GTA-crosslinked scaffolds without miR/NP loading served as a blank control. To identify the osteoinductive activity of miR-29b, miR-NC was bound to AuNPs and loaded on 1% GTA-crosslinked scaffolds, which served as negative controls.

As shown in Fig. 7a, the expression of the osteogenic transcription factor *Runx2*, along with other downstream of *OCN*, *ALP*, and *Col-I* in hMSCs on each MAHS were obviously higher than that of blank and negative control groups during the experiment time frame. This result implied that miR-29b released from the MAHSs upregulated multiple

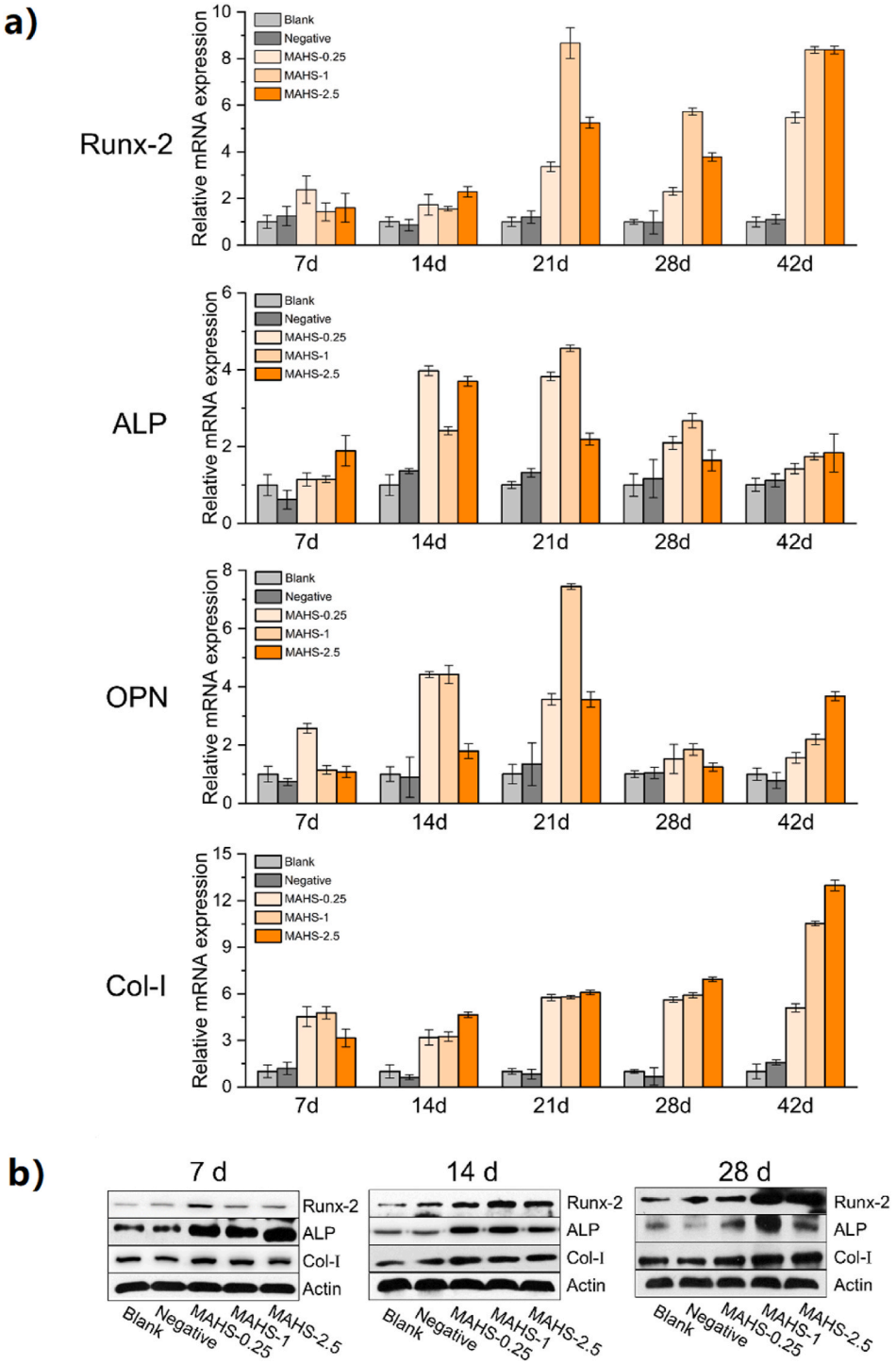

Fig. 7. *In vitro* osteogenesis of hMSCs seeded on each MAHS. (a) Time course changes in osteogenic gene levels in different MAHSs (including *Runx2, ALP, OCN* and *Col-I*) from days 7–42 were determined with real-time PCR. (b) Western blot for Runx2, ALP, Col-I proteins. β-Actin protein (Actin) was used as control. All experiments were carried out in triplicate. n = 4 per group. Data are the mean ± s.d.

osteogenic factors at various osteoblastic differentiation stages of hMSCs *in vitro*. Moreover, the expression levels of osteogenesis-related genes in hMSCs on MAHSs with different cross-linking degrees showed obvious differences. At early stages (days 7 and 14), the levels of these genes in MAHS-0 and MAHS-0.25 groups were higher than those in MAHS-1 and MAHS-2.5 groups, probably owing to the accelerated miR-29b release in the former two groups, which promoted the osteogenesis of hMSCs at an early stage. However, during the matrix maturation period (days 14 and 21), MAHS-1 and MAHS-2.5 were more effective at enhancing expression of the examined genes than MAHS-0 and MAHS-0.25, followed by robust expression in the former groups. During the late mineralization stage (days 28–42), the mRNA expressions of these four markers were sustained at high levels in the MAHS-1 and MAHS-2.5 groups and the MAHS-1 group showed highest osteo-related gene expressions. Contrarily, there was a continued decline in the mRNA levels of these markers in MAHS-0.25 group, which was likely due to the fast release of miR-29b at early stage. Consistently, the western blot results in Fig. 7b also indicated that the sustained delivery of miR-29b

controlled by the mild degradation of MAHS-1 and MAHS-2.5 was more in favor of protein expressions of osteo-related markers, including Runx2, ALP and Col-I than the others.

To validate whether the enhanced osteoblastic differentiation was caused by the bio-function of miR-29b, we examined the expression of miR-29b target, histone deacetylase 4 (HDAC4), at protein levels (Supplementary Fig. S4). HDAC4 is a direct target of miR-29b, which has been demonstrated to reduce transcriptional activity of the bone essential Runx-2, thus functioning as a negative regulator in osteogenesis [39–41]. At day 7, the HDAC4 endogenous protein levels was obviously repressed by MAHS-0.25, while MAHS-1 and MAHS-2.5 showed weak repression on HDAC4 expression. By day 14, all experimental groups showed obvious low level of HDAC4 expression, and the highest inhibition was found in MAHS-0.25 group. At day 28, HDAC4 expression recovered in MAHS-0.25 group, while the protein expression in MAHS-1 and MAHS-2.5 groups consistently remained relatively low levels. Sustained inhibition of miR-29b target was consistent with the time scale of miR/NP release, as shown in Fig. 2f. These results confirmed that miR-29b released form MAHS was capable of sustained expression of its target HDAC4 (a negative regulator in osteogenesis), thus promoting the osteoblastic differentiation.

3.9. *In vivo* degradation

An important property of bone regenerative scaffold materials is their ability to degrade, i.e., the degradation rate of scaffolds must match the rate of new bone formation. For hydrogel materials, the degradation rate can be highly regulated by the crosslinking degree, according to the specific needs of tissue regeneration and repair [42]. It is quite difficult to precisely monitor the *in vivo* degradation rate of each MAHS. However, we could partly observe the degradation of the scaffold based on hematoxylin and eosin (H&E)-stained slides. As shown in Fig. 8, the scaffold fibers were stained as dark purple and thus were easy to distinguish from surrounding tissues. Due to the dehydration-shrinking properties of hydrogels, the dehydration process and paraffin embedding during the sample preparation caused shrinkage and severe deformation of the gel fibers, resulting in partial detachment of fibers from surrounding tissues. After two weeks of implantation, MAHS-0 was totally absorbed by the host, while the other three groups showed varying degrees of degradation but still maintained the whole structure for cell and tissue ingrowth. For MAHS-0.25, MAHS-1 and MAHS-2.5 groups, cell and tissues ingrowth were seen in all sections, indicating that the highly interconnected 3D porous structure facilitated the ingrowth of cells and tissues. There were more cells and tissues observed MAHS-0.25 in group, probably due to more space for ingrowth provided by faster degradation. However, with prolonged implantation (4 weeks), further rapid degradation of MAHS-0.25 made it difficult to provide efficient space and mechanical support for cell and tissue ingrowth, leading to dissociation with surrounding tissues. On the contrary, MAHS-1 and MAHS-2.5 still preserved their 3D structure and supported the ingrowth of cells and tissues. Notably, no obvious mature bone tissue was found around the degraded materials after 4 weeks of implantation. This could possibly be due to the lack of bone forming capacity of the subcutaneous model of heterotopic bone formation, which needs longer treatment duration for bone formation [43]. In addition, few inflammatory cells were found in each group, indicating that the seeded cells and scaffolds had good biocompatibility without triggering the host immune inflammatory response. The results fully verified that the highly interconnected structure as well as the adaptable degradation behavior of scaffolds provided a better environment for neo-tissue formation and expansion.

3.10. *MAHS induced osteogenic differentiation of hMSCs in vivo*

The intriguing *in vitro* osteogenic induction activity of MAHSs bodes well for *in vivo* osteogenesis of hMSCs and bone regeneration. A well-established subcutaneous implantation model in nude mice was used to test whether each MAHS could sustain the delivery of miRNA into hMSCs *in vivo* for a prolonged period of time to consistently promote osteogenic differentiation of hMSCs and new bone formation *in vivo*. Eight weeks after implantation, the newly formed bone was evaluated by micro-CT (Fig. 9). A measurement of the bone volume density, defined as the ratio of bone volume to tissue volume (BV/TV), suggested that there was no appreciable new bone volume in blank and negative groups, demonstrating the critical role of miR-29b in inducing osteogenesis of hMSCs *in vivo*. MAHS-0.25 displayed dramatically decreased new bone volume as compared to MAHS-1 and MAHS-2.5 owing to its fast degradation rate, causing it to fail to provide sufficient support for new tissue formation. The results were consistent with the *in vivo* degradation discussed above. On the contrary, MAHS-1 and MAHS-2.5

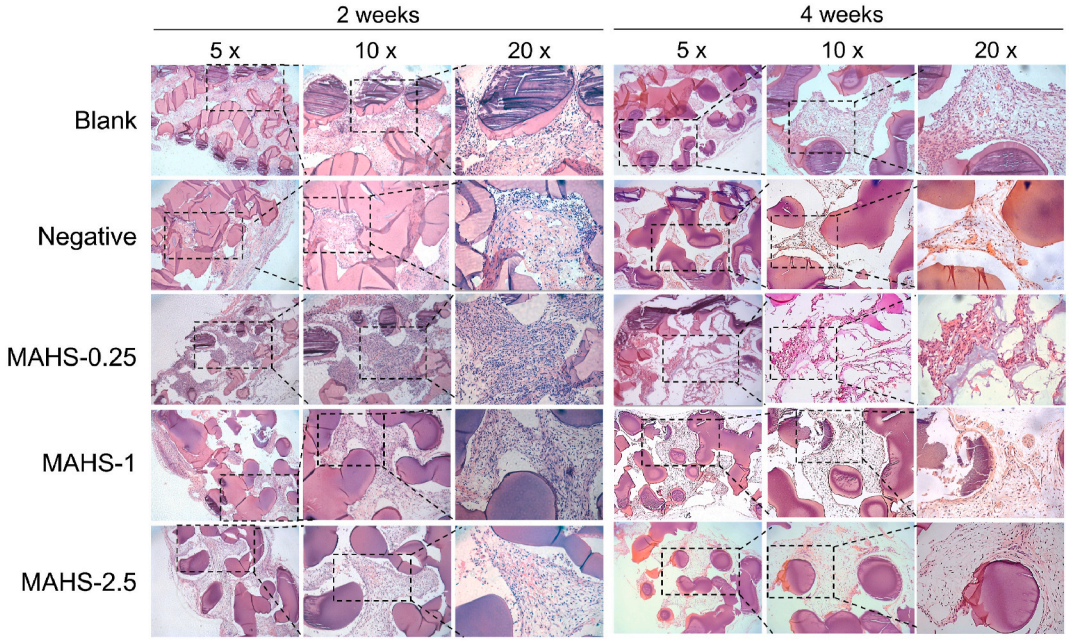

Fig. 8. *In vivo* degradation of MAHSs with different crosslinking degrees assessed by H&E staining.

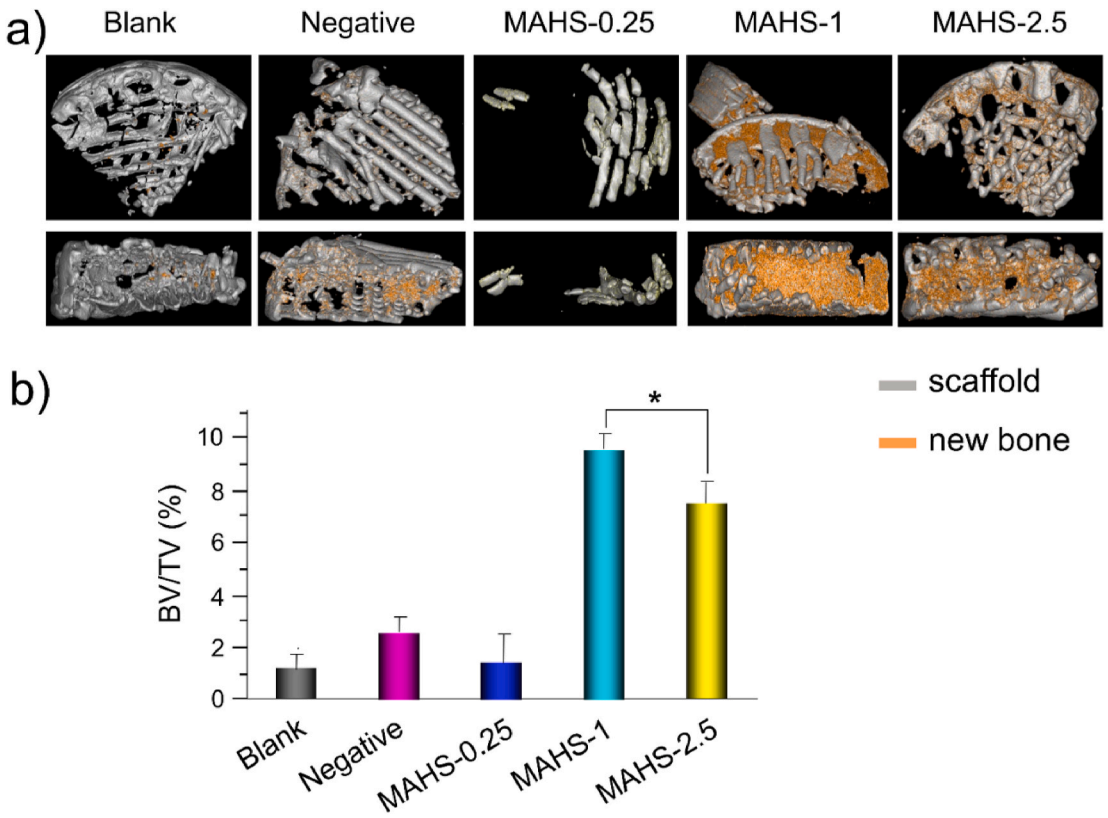

Fig. 9. *In vivo* bone formation in a subcutaneous implantation model. A) Representative micro-CT reconstructions of new bone formation in different hMSCs-seeded MAHS groups. b) The new bone volume and bone mineral density from these groups are quantified. Data are the mean ± s.d., n = 4 per group.

showed about 4-fold higher regenerated volume than that in the controls and MAHS-0.25. Notably, the new bone volume in MAHS-1 was slightly higher than that in the MAHS-2.5, indicating that MAHS-1 displayed better osteo-inductivity than MAHS-2.5 *in vivo*. The results confirm that the balance between miRNA release and scaffold degradation is critical for regulating osteogenesis and bone formation.

OCN, a non-collagenous protein synthesized by osteoblasts during mineralization of bone matrix, is an important indicator of osteogenic activity and bone turnover, accounting for about 10%–20% of non-collagen protein in bone tissue [44]. Immunofluorescence staining for OCN after 8 weeks of implantation is shown in Fig. 8a. There were no obvious green fluorescent spots of OCN in blank and negative groups, indicating that the osteogenesis of hMSCs was not achieved without activation by miR-29b. MAHS-0.25 only showed a few OCN signals, while many green fluorescent spots were observed in MAHS-1 and MAHS-2.5, mainly in the vicinity of the hydrogel fibers, indicating the OCN expression level was relatively high in these two groups. Consequently, these *in vivo* results indicate that the organization of new bone formation is dependent on the interplay between release rate of miRNAs and degradation rate of scaffolds.

In addition, immunofluorescence staining of VEGF, an important signaling protein involved in both vasculogenesis and angiogenesis, is shown in Fig. 10b and Supplementary Fig. S5. Obviously higher expression of VEGF was detected in MAHS-1 and MAHS-2.5 groups compared with control groups and MAHS-0.25 at 4 weeks after scaffold implantation. Furthermore, some red blood cells were clearly found in the vessels in MAHS-1 and MAHS-2.5 groups by H&E staining (Fig. 8). The sufficient blood flow within implantation areas might result from the highly interconnected pore structure and could further stimulate cell proliferation and differentiation, ultimately guaranteeing new bone formation and remodeling. Thus, we found that MAHS-1 and MAHS-2.5 not only displayed superior osteo-inductivity, but also promoted angiogenesis. These collective improvements could lead to enhancement of bone regeneration.

All in all, the MAHS-1 showed optimal pro-osteogenic performance on hMSCs both *in vitro* and *in vivo*. On one hand, MAHS-1 realize sustained delivery of miRNA over 40 days, achieving gene regulation over timeframes commensurate with bone formation. On the other hand, the bio-adaptable degradation rate of MAHS-1 acted in concert with the formation of new bone, as compared with MAHS-0 and MAHS-0.25. The *in vivo* results could indicate feedback to the osteogenic differentiation pathway, which should be further evaluated in additional experiments and studies. Furthermore, immunogenicity of the implanted material remains a major biohazard as considering clinical applications, which might generate severe unexpectable side effects to host bodies. Therefore, further follow-up studies are required to improve the translational potential of this miRNA-activated hydrogel scaffold.

4. Conclusion

In summary, we proposed a miRNA-activated hydrogel scaffold strategy for improving bone regeneration, and thoroughly investigated the joint influence of miRNA release and scaffold degradation on the osteogenesis of hMSCs and on bone formation. This strategy develops a smart matrix composed of two key components: a miRNA nano-delivery system and a porous hydrogel scaffold generated by 3D plotting. Due to the presence of miRNAs, the scaffold can activate the osteoblastic differentiation of hMSCs and induce osteogenesis *in vivo*. By tailoring the crosslinking degree of hydrogels, the release rate of miRNAs and degradation rate of scaffolds can be made to match, thus achieving optimal osteoinductivity for hMSCs osteogenesis and new bone formation. Our findings presented here generalize a promising bioactive scaffold for the bone regeneration.

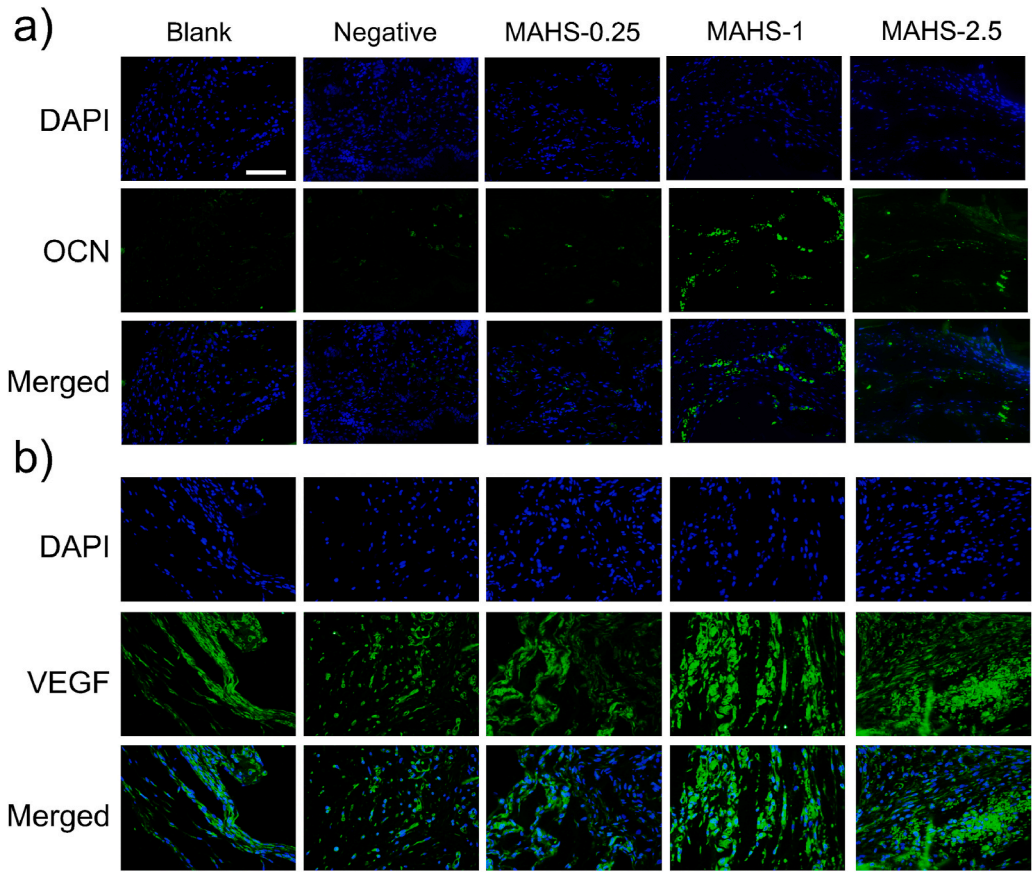

Fig. 10. Immunofluorescence staining for (a) OCN and (b) VEGF in histological sections of each hMSCs-seeded MAHS after subcutaneous implantation for 4 weeks. Scale bars: 500 mm.

Declaration of interests

The authors declare that they have no known competing financial interests or personal relationships that could have appeared to influence the work reported in this paper.

CRediT authorship contribution statement

Ting Pan: generated the idea, Writing – original draft, designed and performed the experiments, Data curation, Formal analysis. **Wenjing Song:** generated the idea, designed and performed the experiments, Writing – original draft, Writing – review & editing, supervised the study, revised and finalized the manuscript, Supervision. **Hongbao Xin:** Writing – review & editing, and supervised the study, Supervision. **Haiyue Yu:** performed the in vivo experiments. **He Wang:** performed the in vivo experiments. **Dandan Ma:** designed the experiments, and performed the in vivo experiments. **Xiaodong Cao:** designed the experiments, Data curation, Formal analysis. **Yingjun Wang:** Funding acquisition, Project administration, Funding acquisition.

Declaration of competing interest

The authors declare that they have no known competing financial interests or personal relationships that could have appeared to influence the work reported in this paper.

Acknowledgements

This research was jointly supported by the National Key R&D Program of China (2018YFC0311103), the National Natural Science Foundation of China (32071333 and 31800832), the Pearl River S&T Nova Program of Guangzhou (201710010195), the Guangdong Scientific and Technological Project (2021A1515010878), the Frontier Research Program of Bioland Laboratory (Guangzhou Regenerative Medicine and Health Guangdong Laboratory, 2018GZR110105008) and the Fundamental Research Funds for the Central Universities.

Appendix A. Supplementary data

Supplementary data to this article can be found online at https://doi.org/10.1016/j.bioactmat.2021.08.034.

References

[1] S.C. Ligon, et al., Polymers for 3D printing and customized additive manufacturing, Chem. Rev. 117 (15) (2017) 10212–10290.
[2] L. Zhang, et al., Three-dimensional (3D) printed scaffold and material selection for bone repair, Acta Biomater. 84 (2019) 16–33.
[3] I. Matai, et al., Progress in 3D bioprinting technology for tissue/organ regenerative engineering, Biomaterials 226 (2020) 119536.
[4] Q. Li, et al., 3D printed silk-gelatin hydrogel scaffold with different porous structure and cell seeding strategy for cartilage regeneration, Bioactive Materials 6 (10) (2021) 3396–3410.
[5] Y. Yan, et al., Vascularized 3D printed scaffolds for promoting bone regeneration, Biomaterials 190–191 (2019) 97–110.
[6] P.S. Gungor-Ozkerim, et al., Bioinks for 3D bioprinting: an overview, Biomaterials Science 6 (5) (2018) 915–946.
[7] G. Huang, et al., Functional and biomimetic materials for engineering of the three-dimensional cell microenvironment, Chem. Rev. 117 (20) (2017) 12764–12850.
[8] T. Pan, et al., 3D bioplotting of gelatin/alginate scaffolds for tissue engineering: influence of crosslinking degree and pore architecture on physicochemical properties, J. Mater. Sci. Technol. 32 (9) (2016) 889–900.
[9] J. Carthew, et al., In situ miRNA delivery from a hydrogel promotes osteogenesis of encapsulated mesenchymal stromal cells, Acta Biomater. 101 (2020) 249–261.
[10] K. Xu, et al., 3D Porous Chitosan-Alginate Scaffold Stiffness Promotes Differential Responses in Prostate Cancer Cell Lines, Biomaterials, 2019, p. 217.

[11] H. Afjoul, A. Shamloo, A. Kamali, Freeze-gelled alginate/gelatin scaffolds for wound healing applications: an in vitro, in vivo study, Materials science & engineering. C, Materials for biological applications 113 (2020) 110957, 110957.
[12] T. Jiang, et al., Engineering bioprintable alginate/gelatin composite hydrogels with tunable mechanical and cell adhesive properties to modulate tumor spheroid growth kinetics, Biofabrication 12 (1) (2020).
[13] M.A. Arriaga, et al., The application of microRNAs in biomaterial scaffold-based therapies for bone tissue engineering, Biotechnol. J. 14 (10) (2019), e1900084.
[14] B. Peng, Y. Chen, K.W. Leong, MicroRNA delivery for regenerative medicine, Adv. Drug Deliv. Rev. 88 (2015) 108–122.
[15] Q. Xie, et al., Effects of miR-146a on the osteogenesis of adipose-derived mesenchymal stem cells and bone regeneration, Sci. Rep. 7 (1) (2017) 42840.
[16] T. Eskildsen, et al., MicroRNA-138 regulates osteogenic differentiation of human stromal (mesenchymal) stem cells in vivo, Proc. Natl. Acad. Sci. U.S.A. 108 (15) (2011) 6139–6144.
[17] J.B. Lian, et al., MicroRNA control of bone formation and homeostasis, Nat. Rev. Endocrinol. 8 (4) (2012) 212–227.
[18] H.-I. Trompeter, et al., MicroRNAs miR-26a, miR-26b, and miR-29b accelerate osteogenic differentiation of unrestricted somatic stem cells from human cord blood, BMC Genom. 14 (2013).
[19] Z. Li, et al., Biological functions of miR-29b contribute to positive regulation of osteoblast differentiation, J. Biol. Chem. 284 (23) (2009) 15676–15684.
[20] W.Y. Lee, et al., miRNA-29b improves bone healing in mouse fracture model, Mol. Cell. Endocrinol. 430 (C) (2016) 97–107.
[21] X. Zhang, et al., Cell-free 3D scaffold with two-stage delivery of miRNA-26a to regenerate critical-sized bone defects, Nat. Commun. 7 (2016) 10376.
[22] W.-J. Song, et al., Gold nanoparticles capped with polyethyleneimine for enhanced siRNA delivery, Small 6 (2) (2010) 239–246.
[23] T. Pan, et al., miR-29b-Loaded gold nanoparticles targeting to the endoplasmic reticulum for synergistic promotion of osteogenic differentiation, ACS Appl. Mater. Interfaces 8 (30) (2016) 19217–19227.
[24] X. Zhao, et al., Collagen-based materials combined with microRNA for repairing cornea wounds and inhibiting scar formation, Biomater Sci 7 (1) (2018) 51–62.
[25] J.F. Martucci, R.A. Ruseckaite, A. Vázquez, Creep of glutaraldehyde-crosslinked gelatin films, Mater. Sci. Eng., A 435–436 (2006) 681–686.
[26] J.F. Martucci, A.E.M. Accareddu, R.A. Ruseckaite, Preparation and characterization of plasticized gelatin films cross-linked with low concentrations of Glutaraldehyde, J. Mater. Sci. 47 (7) (2011) 3282–3292.
[27] J.F. Martucci, R.A. Ruseckaite, Tensile properties, barrier properties, and biodegradation in soil of compression—molded gelatin-dialdehyde starch films, J. Appl. Polym. Sci. 112 (4) (2009) 2166–2178.
[28] B.S. Scopel, et al., Starch-leather waste gelatin films cross-linked with glutaraldehyde, J. Polym. Environ. 28 (7) (2020) 1974–1984.
[29] H. Jin, et al., Polyethylenimine-alginate nanocomposites based bone morphogenetic protein 2 gene-activated matrix for alveolar bone regeneration, RSC Adv. 9 (46) (2019) 26598–26608.
[30] Y. Zhang, et al., Advancements in hydrogel-based drug sustained release systems for bone tissue engineering, Front. Pharmacol. 11 (2020) 622.
[31] M.D. Krebs, O. Jeon, E. Alsberg, Localized and sustained delivery of silencing RNA from macroscopic biopolymer hydrogels, J. Am. Chem. Soc. 131 (26) (2009) 9204–9206.
[32] D.E. Discher, P. Janmey, Y.L. Wang, Tissue cells feel and respond to the stiffness of their substrate, Science 310 (5751) (2005) 1139–1143.
[33] T. Yeung, et al., Effects of substrate stiffness on cell morphology, cytoskeletal structure, and adhesion, Cell Motil Cytoskeleton 60 (1) (2005) 24–34.
[34] E. Saiz, et al., In vitro behavior of silicate glass coatings on Ti6Al4V, Biomaterials 23 (17) (2002) 3749–3756.
[35] J. Song, E. Saiz, C.R. Bertozzi, A new approach to mineralization of biocompatible hydrogel scaffolds: an efficient process toward 3-dimensional bonelike composites, J. Am. Chem. Soc. 125 (5) (2003) 1236–1243.
[36] S.H. Rhee, J. Tanaka, Effect of citric acid on the nucleation of hydroxyapatite in a simulated body fluid, Biomaterials 20 (22) (1999) 2155–2160.
[37] K. Bleek, A. Taubert, New developments in polymer-controlled, bioinspired calcium phosphate mineralization from aqueous solution, Acta Biomater. 9 (5) (2013) 6283–6321.
[38] N.A. Elsayed, S. Zada, N.K. Allam, Mineralization of electrospun gelatin/CaCO3 composites: a new approach for dental applications, Mater. Sci. Eng. C 100 (2019) 655–664.
[39] B.A. Hug, HDAC4: a corepressor controlling bone development, Cell 119 (4) (2004) 448–449.
[40] E.-J. Jeon, et al., Bone morphogenetic protein-2 stimulates Runx2 acetylation *, J. Biol. Chem. 281 (24) (2006) 16502–16511.
[41] Z. Wang, G. Qin, T.C. Zhao, HDAC4: mechanism of regulation and biological functions, Epigenomics 6 (1) (2014) 139–150.
[42] J. Patterson, et al., Hyaluronic acid hydrogels with controlled degradation properties for oriented bone regeneration, Biomaterials 31 (26) (2010) 6772–6781.
[43] Brief review of models of ectopic bone formation, Stem Cell. Dev. 21 (5) (2012) 655–667.
[44] M.L. Zoch, T.L. Clemens, R.C. Riddle, New insights into the biology of osteocalcin, Bone 82 (2016) 42–49.